Supporting Information

Coherent Oscillations in Chlorosome Elucidated by Two-Dimensional Electronic Spectroscopy

Sunhong Jun,[†,‡] *Cheolhee Yang,*[†,‡] *Megumi Isaji,*[§] *Hitoshi Tamiaki,*[§] *Jeongho Kim,**[,⊥] *and Hyotcherl Ihee**[†,‡]

[†]Center for Nanomaterials and Chemical Reactions, Institute for Basic Science (IBS), Daejeon 305-701, Republic of Korea

[‡]Department of Chemistry, KAIST, Daejeon 305-701, Republic of Korea

[§]Graduate School of Life Sciences, Ritsumeikan University, Kusatsu, Shiga 525-8577, Japan

[⊥]Department of Chemistry, Inha University, Incheon 402-751, Republic of Korea

1. Structure of BChl aggregate in chlorosome

Chlorosome was isolated from *Chlorobaculum* (*Cba.*) *limnaeum* 1549 following the protocol reported earlier.[1] A direct image of single chlorosome was observed using atomic force microscopy (AFM),[2] and the mean size of a chlorosome from *Cba. limnaeum* was also determined to be 101 nm × 209 nm × 29 nm (width × length × height) using AFM.[3] Considering the size of chlorosome, it was estimated that a chlorosome contains 2.35×10^5 BChls based on a rod-shaped structure. Although the actual interior of chlorosome is composed of both rod-shaped and lamellar BChl aggregates,[4-5] the rod model has been effective for predicting the number of BChls in a chlorosome. Using the same assumption applied to *Cba. tepidum,* the number of BChls in chlorosome was estimated to be 1.57×10^5 which is very close to value of 1.4×10^5, which was obtained by directly counting the number of BChls using a confocal laser fluorescence microscope.[6] Therefore, we can

conclude that number of BChls in a *Cba. limnaeum* would be about hundreds of thousands as well.

2. Introduction to two-dimensional electronic spectroscopy

Two-dimensional electronic spectroscopy (2D-ES) is an optical analog of two-dimensional NMR technique and can probe the evolution of excitations and couplings between multiple chromophores that absorb at visible frequencies with femtosecond time resolution. 2D-ES makes use of *three* coherent optical pulses to induce third-order polarization signal, $P^{(3)}$. The time ordering of a sequence of three pulses is shown in the inset of Figure S1. The first pulse interacts with the sample system to create coherence between the ground and excited states. After a time delay τ called coherence time, the second pulse generates a population in the excited or ground states. Then, after a time delay T called population time (or waiting time), the third pulse brings the system back to the coherence between the ground and excited states. After a time delay t called rephasing time, the third-order signal (called photon echo) is radiated in a phase-matched direction ($k_s = k_1 + k_2 - k_3$). The emitted signal is measured as a function of the three time delays τ, T, and t, and the measured time-domain data $S_{2D}(\tau, T, t)$ is Fourier transformed with respect to τ and t into a complex-valued two-dimensional spectrum, $S_{2D}(\omega_\tau, T, \omega_t)$ for each T value. The real part of the 2D spectrum corresponds to transient changes in the absorption of the sample at a probe frequency ω_t induced by an excitation frequency ω_τ after the time period T. In contrast, the imaginary part describes transient changes in the refractive index of the sample. In other words, ω_τ and ω_t correspond to "absorption" and "emission" frequencies, respectively, at an instant T. The peaks on the diagonal correspond to linear absorption spectrum and the peaks off the diagonal (called cross peaks) represent coupling and energy transfer between the states with the transition frequencies of ω_τ and ω_t. The theory and experiment of 2D-ES are described in detail elsewhere.[7-8]

The 2D spectrum can be decomposed into two components, rephasing (R) and nonrephasing (NR) spectra. The R and NR components are obtained by Fourier transforming the $S_{2D}(\tau, T, t)$ data for $\tau > 0$ and $\tau < 0$, respectively. As can be seen in Figure S2, the peaks are elongated along the diagonal in the R spectrum while the peaks of NR spectrum are aligned perpendicular to the diagonal. From previous theoretical and experimental studies, it has been demonstrated that the R and NR spectra give complementary information on the

origin of coherent oscillations of 2D spectra with respect to T.[9-11] To distinguish the origin of coherent oscillations observed in the 2D spectra of chlorosome, we employed the comparative test between R and NR spectra as detailed in the main text.

3. Experimental methods

The 2D-ES measurement was performed using a setup based on the diffractive optic.[12-13] Briefly, the 800 nm pulses of 50 fs duration were generated from the 1-kHz regenerative amplified Ti:sapphire laser (Coherent Legend Elite seeded by Vitesse) and converted to visible wavelengths by a home-built, all-reflective-optic noncollinear optical parametric amplifier (NOPA). The NOPA output pulses of 720 nm center wavelength and 80 nm bandwidth were sent to a fused-silica prism compressor, whereby the dispersion of the transmissive optics in the 2D-ES setup were pre-compensated. Then, the compressed laser pulses were sent to a 2D-ES setup shown in Figure S1. A beam of the pulse was focused on a diffractive optic element (DO; Holoeye DE228) by a concave parabolic mirror of 50 cm focal length and split into four beams, which are the first-order diffraction of the input beam. The four beams were collimated and focused into the sample by a pair of concave parabolic mirrors (of 25 cm focal length) aligned in a symmetric geometry so that any comatic aberration can be prevented. Three beams (1 – 3) were used to induce the 3rd-order polarization signal, while beam 4 was attenuated by a factor of 10^3 using a neutral density filter and used as the local oscillator (LO). The time delays between the pulses 1, 2 and 3 were controlled by a pair of wedges (1° tilt angle) inserted in antiparallel orientation. By translating only one of the wedge pair using a motorized stage, the time delay can be changed with the accuracy of ~2.7 attoseconds. For the 2D-ES measurement, photon echo signal was irradiated in the $k_s = -k_1 + k_2 + k_3$ phase-matched direction, one corner of the BOXCARS geometry. The LO field (beam 4), which is collinear with the signal field, mixes with the signal, enabling the phase-sensitive heterodyne detection using the spectral interferometry. The spectral interference fringes between the signal and the LO were recorded with a spectrograph and a CCD while scanning the time delay between pulse 1 and 2 (coherence time, τ), and the delay between pulse 2 and 3 (population time, T). The coherence time τ was varied from –125 fs to +125 fs by 0.25 fs increment, and the population time T was varied from 0 to 480 fs by 5 fs increment. We obtained the absorption frequency ω_τ by Fourier transforming the measured signal along τ axis, while the emission frequency, ω_t is directly obtained by the dispersed detection using a combination of the spectrograph and the CCD,

thus giving a 2D spectrum. The time resolution of the experiment was determined to be 15 fs at the sample position from a non-resonant transient grating measurement of pure solvent (carbon tetrachloride). The frequency-resolved pump-probe spectra were separately measured at various population times using the pulses 1 and 2 as pump and probe pulses, respectively. The 2D spectra were phased by comparing the pump-probe spectra and the projection of 2D spectra onto ω_t axis at each T.

Chlorosomes were isolated from *Cba. limnaeum* 1549, which contain BChl *e* molecules.[2] We prepared a diluted sample solution in a 30:70 (v/v) mixture of 50 mM Tris–HCl buffer and glycerol and added $Na_2S_2O_4$ as reductant. The optical density of the sample solution was 0.3 in a sandwich-type sapphire cell of 0.2 mm optical path length. During the measurement, the sample was kept at 77 K using a cryostat (JANIS VPF-100) with liquid nitrogen as coolant.

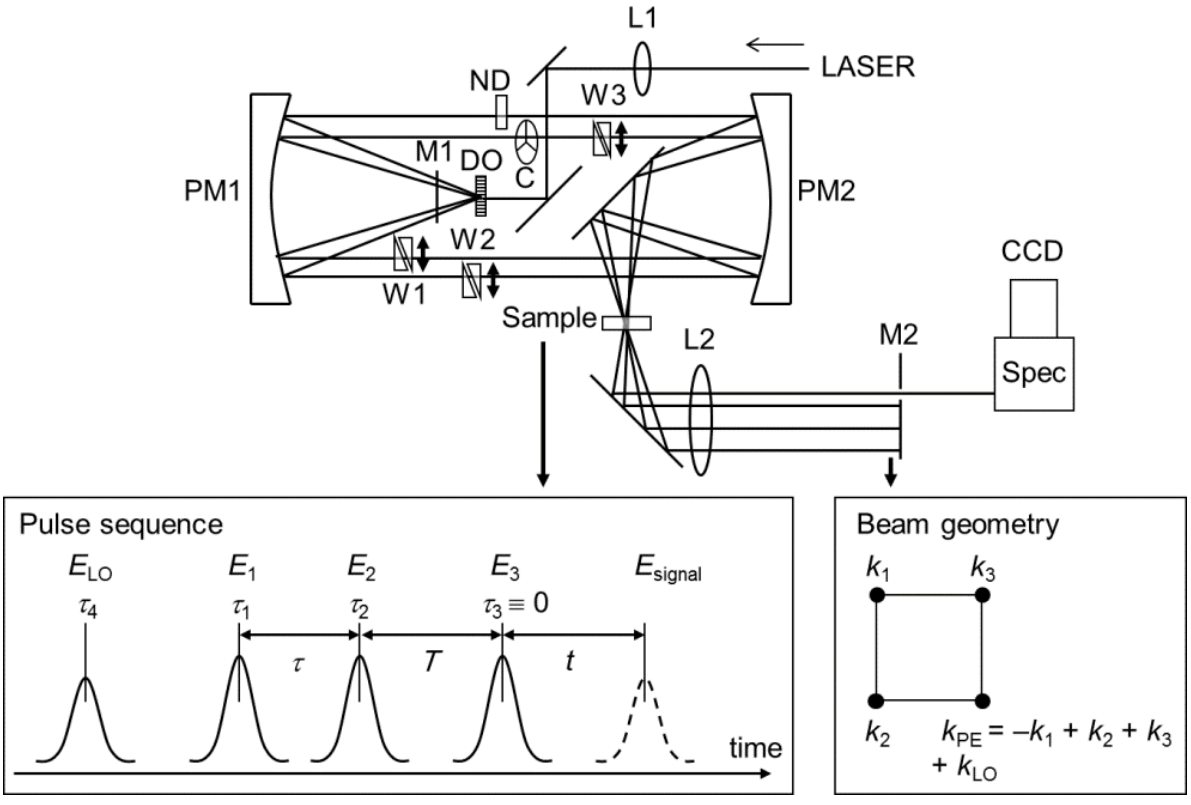

Figure S1. Experimental setup for 2D electronic spectroscopy. A beam of optical pulse is focused onto a diffractive optic (DO) by a 50 cm f.l. concave spherical mirror (L1) to generate four beams of pulses, E_1, E_2, E_3, and E_{LO}, diffracted at first order. The four beams transmitted through the mask (M1) are collimated and focused onto the sample by a pair of 25 cm f.l. paraboloid mirrors (PM1, PM2). The time delays between the pulses, t_1, t_2, and t_3, are varied with interferometric precision by moving

one of each glass wedge pair (W1, W2, and W3) inserted into the E_1, E_2, and E_3 optical beams. The E_1, E_2, E_3, and E_{LO} pulses are incident on the sample with k_1, k_2, k_3, and k_{LO} wavevectors at τ_1, τ_2, τ_3, and τ_4 arrival times, respectively. Time zero is defined at the center of the pulse 3, i.e. $\tau_3 = 0$. The third-order signal (k_s) is radiated in the direction of $-k_1 + k_2 + k_3$, the same direction as k_{LO} in the four-beam BOXCARS geometry. The LO pulse is attenuated by a factor of 10^3 using a neutral density filter (ND) and always precedes the other three pulses by the time delay, t_4, that was set to be $t_4 = \tau_4 \approx -500$ fs. After being collimated by a 25 cm f.l. concave spherical mirror (L2), the heterodyned signal is detected as a spectral interferogram along ω_t axis by a combination of spectrograph and CCD array detector.

4. FT resolution of 2D FT spectra

The frequency resolution of ω_T is determined by the time step (5 fs in this measurement) and the number of points along T axis (97 population time points from 0 to 480 fs) and was about 70 cm^{-1} in our measurement. Thus, a slice of the spectral solid at a specific frequency can be regarded as the integration of the slices along ω_T axis with ~70 cm^{-1} bandwidth around the corresponding center frequency.

5. Low-frequency oscillations in 2D spectrum

As can be seen in Figure S2 and S3a, for both R and NR components, the 2D FT maps for the 140 cm^{-1} oscillation have almost the same shape as the 2D spectra at $T = 0$ fs. This similarity indicates that the slow oscillation is observed at every (ω_τ, ω_t) location where the third-order spectroscopic signal is induced. To investigate the origin of this oscillation, we examined the line-slices of the 3D spectral solid along ω_T axis (that is, FT spectrum with respect to ω_T) at four selected diagonal-peak (DP) and cross-peak (CP) points on the 2D spectra: CP21 (1.710 eV, 1.693 eV), DP11 (1.693 eV, 1.693 eV), CP12 (1.693 eV, 1.710 eV), and DP22 (1.710 eV, 1.710 eV). We selected these points because the 2D FT maps have significant amplitudes at these diagonal and off-diagonal locations on the 2D spectrum and the difference between the absorption and emission frequencies, $|\omega_\tau - \omega_t|$, associated with CP12 and CP21 is ~140 cm^{-1}. In principle, a quantum beat of a certain frequency is expected to appear at the locations where $|\omega_\tau - \omega_t|$ matches the beat frequency. The line-slices at the selected points were obtained by Fourier transform after modest zero padding in the T axis in order to allow for finite time interval and limited time range used in our measurement. In the line-slices of the spectral solid in Figure S3b, a positive peak is observed clearly in the ω_T frequency region of

100 – 170 cm^{-1} at all the selected points on both R and NR spectra, suggesting that this oscillation originates from vibrational coherence.

To further characterize the oscillations observed in the 2D spectra, we applied linear prediction singular value decomposition (LPSVD) analysis to the time-domain traces at the selected points. In this method, the time-domain signal is fit by a linear combination of exponentially decaying oscillatory functions. The time-domain traces and their major LPSVD components are shown in Figure S4, and the complete LPSVD fit parameters are listed in Table S1. From the LPSVD analysis, we found that the most pronounced oscillations in the time-domain traces are well fit by a LPSVD component with the frequency of 100 – 170 cm^{-1} and the dephasing time of hundreds of femtoseconds. This low-frequency oscillation is observed at all the selected points on both R and NR spectra. As expected, the frequencies of the oscillations extracted from the time-domain traces match well with $|\omega_\tau - \omega_t|$ at CP12 and CP21 within approximately 70 %. Therefore, we conclude that the oscillation of 140 cm^{-1} frequency arises from vibrational coherence, not from electronic coherence. In addition to the 140 cm^{-1} oscillation, we observe a slower oscillation of 50 – 100 cm^{-1} frequency as a negative peak in the line slices at all the selected points (see Figure S3). The 2D FT maps for this slower oscillation are shown in Figure S5.

In the previous studies using transient absorption, photon echo, and resonance Raman spectroscopies,[14-19] the oscillations with the frequencies of 50 – 250 cm^{-1} have been observed. In those studies, these low-frequency oscillations were assigned to vibrational coherences created in the ground state of BChl aggregates. In our data, however, the oscillations of similar frequencies are also observed in the negative ESA regions in the 2D spectra with the phase shift of ~180° from the ones in the positive GSB and SE regions, suggesting the participation of vibrational coherence in the excited electronic state. Therefore, the oscillation of 140 cm^{-1} frequency is likely to arise from the vibrational coherences generated in the ground or excited state of chlorosome.

6. Locations of low-frequency oscillations in 2D spectrum

Here we note that it can be confusing that the low-frequency oscillations of 50 – 170 cm^{-1} frequencies are also observed at many locations where $|\omega_\tau - \omega_t|$ do not match the frequency of the time-domain oscillation along *T*. For example, these slow oscillations are also observed at the points selected for the examination of 620 cm^{-1} oscillation as shown in Figure S6. This observation disobeys the principle that there should be a quantum beat of only one frequency

given by $|\omega_\tau - \omega_t|$ at a certain location in the 2D spectrum. This issue, the presence of multiple frequencies at a specific location in the 2D spectrum, has been already reported in a previous 2D-ES study on a phycobiliprotein LHC.[9] That study interpreted this issue by proposing that a specific element of the density matrix defined by a combination of absorption (ω_τ) and emission (ω_t) frequencies is not separately measurable by 2D-ES. Instead, the dynamics along T measured by 2D-ES are given by the time evolution of the full density matrix, which is described by a set of coupled differential equations, leading to the appearance of the oscillations with multiple frequencies at a certain location in the 2D spectra.

7. Locations of 620 cm^{-1} oscillation in 2D spectrum

We speculated why the electronic coherence of ~620 cm^{-1} is observed among the particular pair of exciton states with the energies of 1.761 eV and 1.685 eV. A chlorosome has manifold of exciton states formed by hundreds of thousands of constituent BChl molecules. Therefore, besides this specific pair of states, there can be many pairs of exciton states that have the energy difference of ~620 cm^{-1} between each other and thus yield the coherence beats of the same frequency. To account for the locations of the electronic coherence in the 2D spectrum observed in our experiment, we note that the Q_y absorption band has a symmetric bell shape around a peak (~1.72 eV at 77 K) and the transition energies of the pair of exciton states, 1.761 eV and 1.685 eV, are apart from the peak by about the same amount (~0.04 eV). The magnitude of coherence created between a pair of states (and thus the cross-peak intensity in a 2D spectrum) is dependent on the magnitudes of transition dipoles of the two involved exciton states. Therefore, as long as electronic coherence is generated among a pair of exciton states with the energy difference of ~620 cm^{-1}, a pair of states with nearly equal oscillator strengths will generate the maximum magnitude of coherence, which is the case in our experimental result.

8. Asymmetric shape of 2D spectra

It should be noted that, for the upper cross-peak point (CP12) and the upper diagonal-peak point (DP22), the amplitude contrast between R and NR components of 2D FT spectra is not as high as for the lower cross peak (CP21) and the lower diagonal peak (DP11). Such asymmetry may be associated with the nature of downhill energy transfer occurring in chlorosomes. In general, in the 2D spectra of LHCs, the locations involving higher-energy emitting states have smaller amplitudes than the locations of lower-energy emitting states,

resulting in the 2D spectrum of asymmetric overall shape with respect to the diagonal. Similarly asymmetric patterns with higher signal amplitudes in the lower-energy emitting states have been observed in the 2D spectra of other LHCs[9, 20-23] and molecular nanotubes.[24-25]

9. Linear prediction singular value decomposition of the oscillations

Fast Fourier transform (FFT) is commonly used to analyze the spectral properties of oscillatory components in time-domain data. However, FFT is not suitable when the measured time-domain data does not span a long period in time, has limited time resolution, or has a low signal-to-noise ratio. In that case, FFT can cause spectral distortion and poor spectral resolution. Our data have a limited number of population time points (97 points) in a limited time window (480 fs), giving the spectral resolution of only ~70 cm^{-1}, and the oscillatory components of interest have inherently small amplitude. In order to confirm the spectral properties of the oscillatory components extracted from these data using FFT, we applied modified linear prediction singular value decomposition (LPSVD) method.[26]

The LPSVD method fits the time-domain signal by a model function consisting of a finite number of exponentially decaying sinusoids:

$$S(\omega_\tau, T, \omega_t) = \sum_i A_i \exp(-T/\tau_i)\cos(2\pi c\tilde{\nu}_i t + \varphi_i) \quad (1)$$

where A_i, τ_i, $\tilde{\nu}_i$, and φ_i are the amplitude, damping (or dephasing) time constant, frequency, and phase of a sinusoidal component *i*. This method is based on two major principles: singular value decomposition (SVD) and estimation of linear prediction coefficients. Since LPSVD is a non-iterative fitting algorithm, starting values of the model parameters or iterations to find convergence at some set of parameters are not needed. Instead, direct calculations using linear algebra are used to determine the fitting parameters (that is, amplitude, damping time, frequency, and phase for each sinusoidal component) in Eq. (1). SVD is used to distinguish between signal and noise. These aspects of LPSVD allow us to analyze the time-domain signals with low signal-to-noise ratio and limited number of data points. In addition, the LPSVD method can extract the damping time constant and phase of each sinusoid, which is difficult in FFT. However, in turn, the results of LPSVD fits must be judged carefully so that the fits to noise can be discarded.

For the data analysis, we used the entire 2D data set from T = 0 to T = 480 fs with 5 fs step size (97 points). LPSVD was performed for the time-domain data at the selected points (in

Figure 2a in the main text or Figure S3a) independently from each other. To optimize the number of oscillatory components needed for the fits of individual time-domain traces, we increased the number of sinusoidal functions one by one to improve the overall fitting quality and stopped when the experimental time trace was overfit (that is, when noise-like oscillations were fit). For the 140 cm^{-1} and 620 cm^{-1} oscillations, the time-domain traces and their major LPSVD components are shown in Figures S4 and S6, respectively, while the complete fit parameters are listed in Tables S1 and S2, respectively.

From the LPSVD analysis of time traces at CP21 (1.710 eV, 1.693 eV), DP11 (1.693 eV, 1.693 eV), CP12 (1.693 eV, 1.710 eV), and DP22 (1.710 eV, 1.710 eV) in Figure S3a, we found that the most pronounced oscillation observed in the time-domain traces are well fit by a LPSVD component with the frequency of 100 – 170 cm^{-1} and the dephasing time of hundreds of femtoseconds. The frequencies of the oscillations extracted from the time-domain traces match well with $|\omega_\tau - \omega_t|$ at CP12 and CP21 within approximately 70 %. In addition to the 140 cm^{-1} oscillation, we observe a slower oscillation of 50 – 100 cm^{-1} frequency as a negative peak in the line-slices at all the selected points (see Figure S4). The opposite sign of the peak corresponding to this lower-frequency oscillation means that this slower oscillation is out of phase by about 180° from the 140 cm^{-1} oscillation. The 2D FT map for the oscillation of 70 cm^{-1} frequency shown in Figure S5 shows that the 70 cm^{-1} oscillation appear at nearly the same locations as the 140 cm^{-1} oscillation but with the opposite sign. Also, the components with the frequency of 50 – 100 cm^{-1} were identified with the dephasing time of a few picoseconds and the phase shifted by 180° – 260° from the 140 cm^{-1} component.

From the LPSVD analysis of time traces at CP21 (1.761 eV, 1.685 eV), DP11 (1.685 eV, 1.685 eV), CP12 (1.685 eV, 1.761 eV), and DP22 (1.761 eV, 1.761 eV) in Figure 2a (in the main text), we identified a LPSVD component with ~620 cm^{-1} frequency and ~45 fs dephasing time constant. Notably, this oscillatory component is observed only at the CPs of the R spectrum and at the DPs of the NR spectrum. As expected, the frequencies of the oscillations extracted from the time-domain traces match well with $|\omega_\tau - \omega_t|$ at CP21 and CP12 within approximately 85 %. For CP21, the R component has a major LPSVD component of 645 ± 61 cm^{-1} frequency and 47 ± 17 fs dephasing time constant, while the NR component does not give any component around this frequency. For DP11, the NR component exhibits a major LPSVD component with the frequency of 602 ± 43 cm^{-1} and the

dephasing time constant of 45 ± 15 fs, while the R component does not give any component at this frequency. For CP12 and DP22, the oscillations in the time-domain traces are much smaller in amplitude than for CP21 and DP11 for the same reason described above. Still, we can extract the LPSVD components with frequencies near 620 cm^{-1}, only from the R component at CP12 and the NR component at DP22. These LPSVD components for CP12 (R) and DP22 (NR) have slightly larger frequencies (693 cm^{-1} and 718 cm^{-1}) and longer dephasing time constants (83 fs and 143 fs) than the oscillatory components from the CP21 (R) and DP11 (NR). This discrepancy in the frequency and the dephasing time seems to be the error caused by smaller signal amplitudes (and thus lower signal-to-noise ratio) at CP12 and DP22.

10. Global fitting analysis of the oscillations

As described in the previous section, we performed the LPSVD analysis for individual time traces at CPs and DPs independently and showed that the oscillatory component of ~620 cm^{-1} frequency is present only at CPs of the R spectrum and DPs of the NR spectrum. In principle, when electronic or vibrational coherence is created, a conjugate pair of CPs with the same value of $|\omega_\tau - \omega_t|$ (or their corresponding DPs) should exhibit the oscillation of the same frequency and the same dephasing rate. However, from the LPSVD analysis, we can find some discrepancies in the frequency and the dephasing time among the time traces and attributed it to smaller signal amplitudes at CP12 and DP22. In order to better describe the temporal behavior of the oscillations, we also performed the least-squares fitting globally for the oscillatory time traces at CPs and DPs. For global fitting, we used a model function consisting of exponentially decaying sinusoids as in Eq. (1), but each of the sinusoids were forced to have the same oscillation frequency and damping time for all the selected time traces. Based on the results of LPSVD analysis, we grouped the time traces at CP21 (R), DP11 (NR), CP12 (R), DP22 (NR) together and globally fit them by the sinusoids sharing the oscillation frequencies and damping times. Also, we grouped the other time traces, CP21 (NR), DP11 (R), CP12 (NR), and DP22 (R), together and globally fit them using the sinusoids sharing the oscillation frequencies and damping times. To fit the experimental data, the squared sum of the deviation between the experimental data and the model function at all the time points was minimized using the Levenberg-Marquardt algorithm. The fits for the all the time traces at the selected CPs and DPs in Figure 2 are shown in Figure 3 and the optimized parameters are shown in Table S3.

As can be seen in Figure 3, all the time traces were fit well using three exponentially decaying sinusoids. To determine the number of sinusoidal components needed for the fit, we increased the number of components one by one to improve the overall fitting quality and stopped when the experimental time trace was overfit (that is, when noise-like oscillations were fit). We can see that the oscillatory component of 654 cm^{-1} frequency and 60 fs damping time is the major component at the CPs of the R spectrum and the DPs of the NR spectrum. In contrast, at other CPs and DPs, we were not able to find any oscillation of such high frequency. Therefore, the results of the global fitting analysis are in agreement with those of the LPSVD analysis.

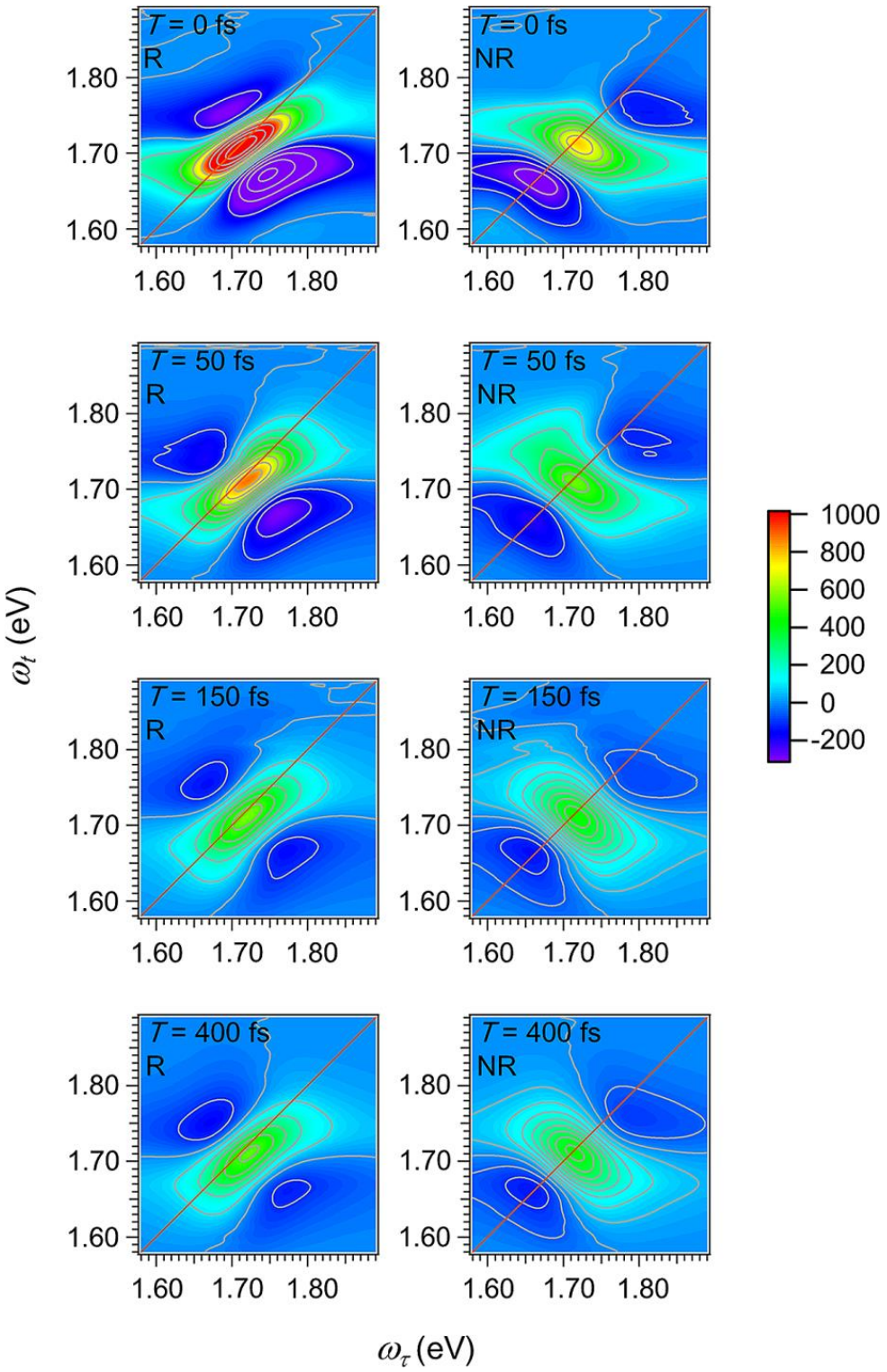

Figure S2. Rephasing (R) and nonrephasing (NR) components of 2D spectra at the population times of T = 0, 50, 150, and 400 fs.

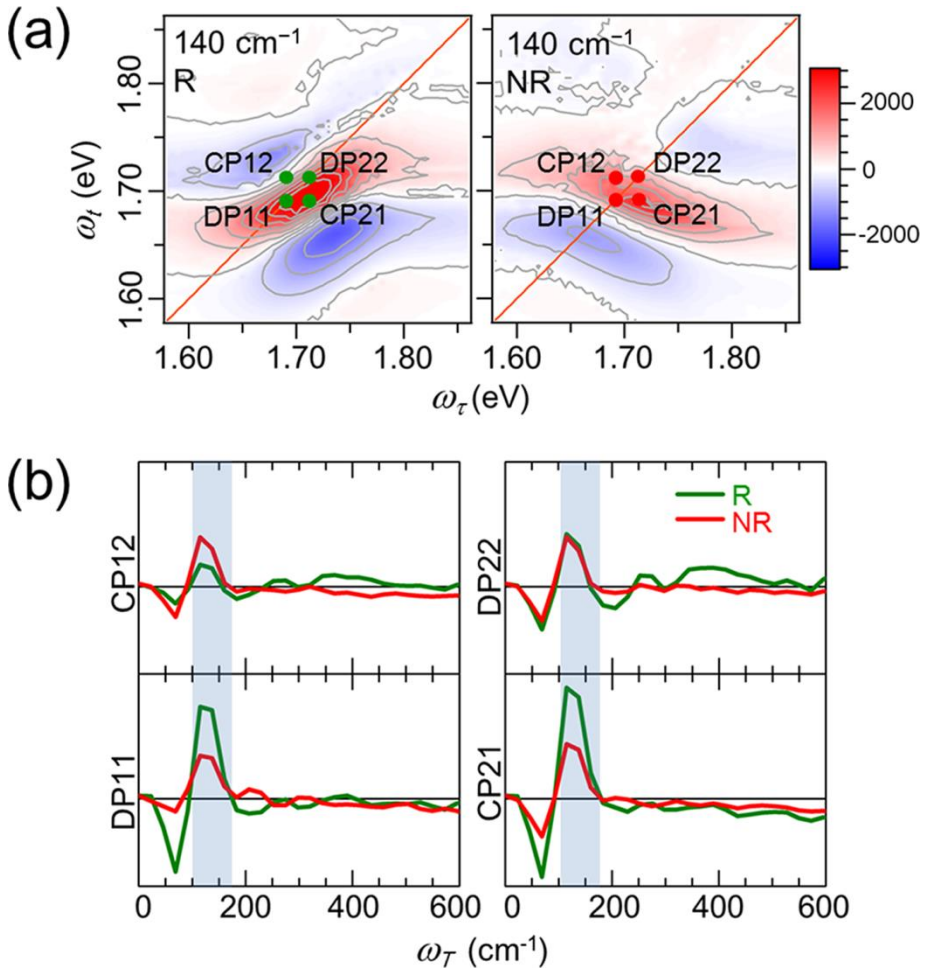

Figure S3. (a) 2D FT maps of rephasing (left) and nonrephasing (right) components for the 140 cm^{-1} oscillation. For both rephasing and nonrephasing components, the shapes of the 2D spectrum in Figure S2 and the 2D FT map are very similar to each other, implying that the oscillation arises from vibrational coherence generated in the ground or electronic excited state of chlorosome. (b) Line-slices of the 3D spectral solid along ω_T axis (that is, FT spectrum with respect to ω_T) for rephasing (green line) and nonrephasing (red line) components at four selected points, CP12, CP21, DP11, and DP22, on the 2D spectra as indicated by green (rephasing) and red (nonrephasing) points on the 2D FT maps shown in (a).

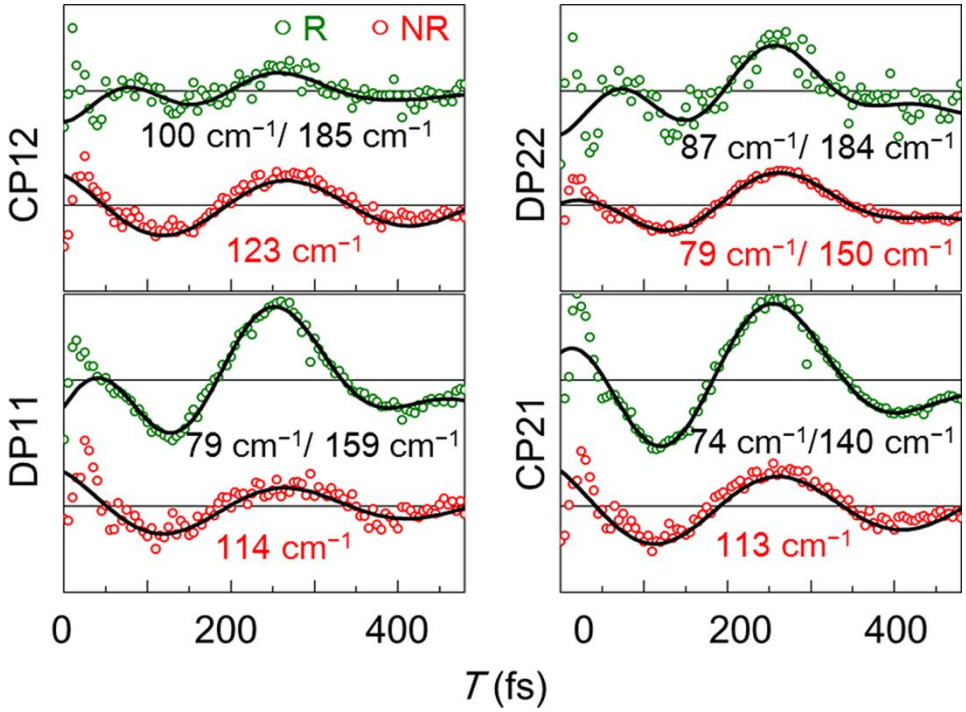

Figure S4. Time-domain traces for the rephasing (green circles) and nonrephasing (red circles) components at the selected points in Figure S3a shown together with their corresponding major LPSVD components (black lines). The frequency of each LPSVD component is written together below each time-domain trace.

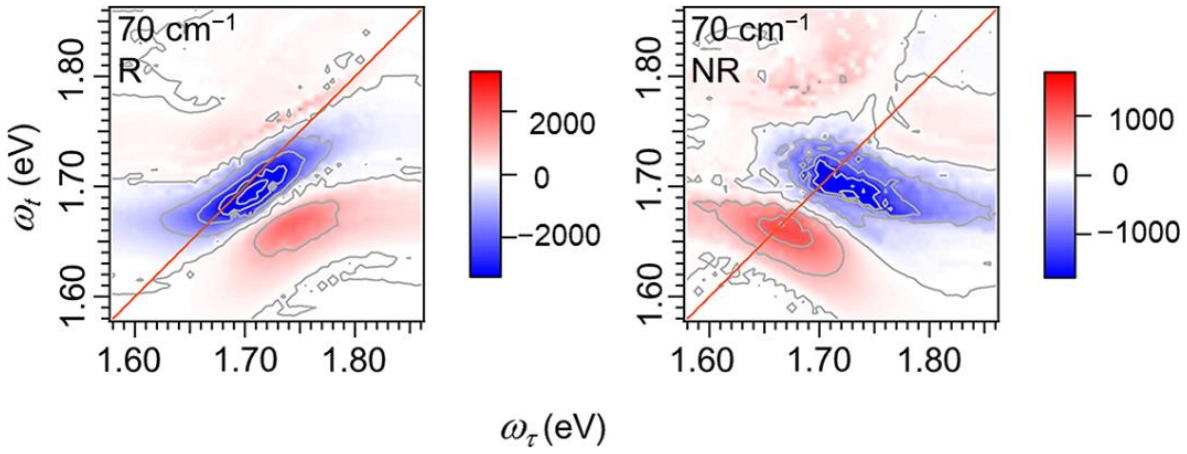

Figure S5. 2D FT maps of rephasing (left) and nonrephasing (right) components for the 70 cm^{-1} oscillation.

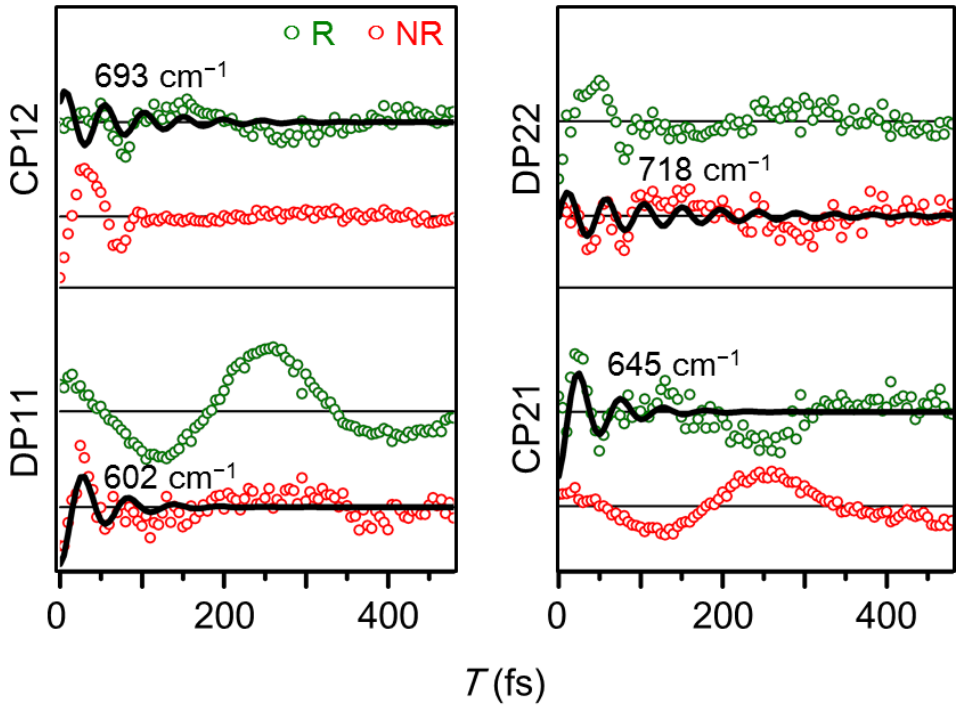

Figure S6. Time-domain traces for the rephasing (green circles) and nonrephasing (red circles) components at the selected points in Fig. 2a. The major LPSVD components with frequencies of ~620 cm^{-1} (black lines) are shown together. The frequency of each LPSVD component is indicated above the time trace.

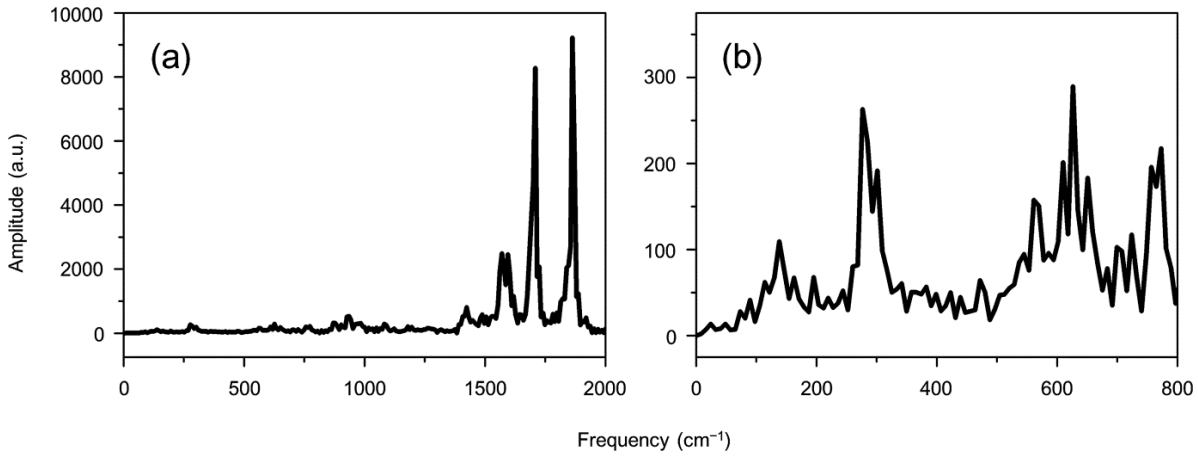

Figure S7. (a) Spectral density calculated for BChl aggregate consisting of multilayered rolls. (b) Expanded view of the spectral density in the frequency region of 0 – 800 cm^{-1}. Adapted from Ref. [27] and reproduced.

Table S1. Parameters obtained from the LPSVD analysis of the oscillations presented in Figure S4

Location	Frequency (cm^{-1})	Dephasing (fs)	Amplitude (a.u.)	Phase (degrees)
CP12	(ω_τ, ω_t) = (1.693 eV, 1.710 eV)			
R	100	677	0.35	–85
	185	152	0.65	170
NR	113	765	1.00	–32
DP22	(ω_τ, ω_t) = (1.710 eV, 1.710 eV)			
R	87	3105	0.30	–112
	184	346	0.39	149
NR	79	1212	0.16	–124
	150	696	0.20	56
DP11	(ω_τ, ω_t) = (1.693 eV, 1.693 eV)			
R	79	1071	0.56	–139
	159	354	0.63	76
NR	114	364	0.39	–27
CP21	(ω_τ, ω_t) = (1.710 eV, 1.693 eV)			
R	74	1277	0.49	31
	140	321	0.84	–153
NR	113	625	0.46	–38

Table S2. Parameters obtained from the LPSVD analysis of the oscillations presented in Figure S6

Location	Frequency (cm^{-1})	Dephasing (fs)	Amplitude (a.u.)	Phase (degrees)
CP21	(ω_τ, ω_t) = (1.761 eV, 1.685 eV)			
R	77	861	0.21	13
	174	285	0.25	–73
	357	274	0.09	103
	645	47	0.59	175
NR	78	410	0.20	–124
	157	982	0.31	33
DP11	(ω_τ, ω_t) = (1.685 eV, 1.685 eV)			
R	77	802	0.98	151
	147	680	0.72	19
NR	106	789	0.13	–48
	228	197	0.1	84
	602	45	0.56	–169
CP12	(ω_τ, ω_t) = (1.685 eV, 1.761 eV)			
R	104	477	0.18	–141
	178	178	0.99	10
	496	152	1.69	127
	693	83	0.30	–52
NR	91	482	0.06	–59
	434	30	1.74	165
	812	11	1.43	15
	845	48	0.37	137
DP22	(ω_τ, ω_t) = (1.761 eV, 1.685 eV)			
R	113	426	0.11	9
	440	63	0.32	–148
	870	45	0.16	157
NR	120	962	0.08	–163
	718	143	0.14	91

Table S3. Fit parameters obtained from the global fitting analysis of the oscillations presented in Figure 3 in the main text.

Location	Frequency (cm^{-1})	Dephasing (fs)	Amplitude (a.u.)	Phase (degrees)
CP21	(ω_τ, ω_t) = (1.761 eV, 1.685 eV)			
R	108 ± 3	1061 ± 552	43 ± 6	102 ± 12
	206 ± 11	91 ± 14	105 ± 16	–10 ± 13
	654 ± 7	60 ± 8	95 ± 13	–160 ± 8
NR	102 ± 2	5.38×10^{25}	40 ± 2	–62 ± 8
	169 ± 4	1048 ± 760	18 ± 4	64 ± 33
	402 ± 8	54 ± 4	6 ± 6	–116 ± 50
DP11	(ω_τ, ω_t) = (1.685 eV, 1.685 eV)			
R	102 ± 2	5.38×10^{25}	93 ± 4	–69 ± 9
	169 ± 4	1048 ± 760	47 ± 12	78 ± 5
	402 ± 8	54 ± 4	17 ± 8	71 ± 20
NR	108 ± 3	1061 ± 552	27 ± 4	–51 ± 11
	206 ± 11	91 ± 14	28 ± 10	–93 ± 7
	654 ± 7	60 ± 8	104 ± 12	–153 ± 7
CP12	(ω_τ, ω_t) = (1.685 eV, 1.761 eV)			
R	108 ± 3	1061 ± 552	27 ± 5	165 ± 10
	206 ± 11	91 ± 14	48 ± 9	36 ± 15
	654 ± 7	60 ± 8	18 ± 10	–54 ± 31
NR	102 ± 2	5.38×10^{25}	7 ± 1	–16 ± 12
	169 ± 4	1048 ± 760	3 ± 2	18 ± 29
	402 ± 8	54 ± 4	140 ± 8	153 ± 4
DP22	(ω_τ, ω_t) = (1.761 eV, 1.685 eV)			
R	102 ± 2	5.38×10^{25}	12 ± 1	–15 ± 9
	169 ± 4	1048 ± 760	4 ± 2	96 ± 23
	402 ± 8	54 ± 4	66 ± 5	–179 ± 6
NR	108 ± 3	1061 ± 552	17 ± 4	167 ± 13
	206 ± 11	91 ± 14	18 ± 10	–26 ± 29
	654 ± 7	60 ± 8	27 ± 10	60 ± 20

References

(1) Mizoguchi, T.; Kim, T.-Y.; Sawamura, S.; Tamiaki, H. Pressure-Induced Red Shift and Broadening of the Q_y Absorption of Main Light-Harvesting Antennae Chlorosomes from Green Photosynthetic Bacteria and Their Dependency Upon Alkyl Substituents of the Composite Bacteriochlorophylls. *J. Phys. Chem. B* **2008,** *112*, 16759-16765.

(2) Tamiaki, H.; Tateishi, S.; Nakabayashi, S.; Shibata, Y.; Itoh, S. Linearly Polarized Light Absorption Spectra of Chlorosomes, Light-Harvesting Antennas of Photosynthetic Green Sulfur Bacteria. *Chem. Phys. Lett.* **2010,** *484*, 333-337.

(3) Martinez-Planells, A.; Arellano, J.; Borrego, C.; López-Iglesias, C.; Gich, F.; Garcia-Gil, J. Determination of the Topography and Biometry of Chlorosomes by Atomic Force Microscopy. *Photosynth. Res.* **2002,** *71*, 83-90.

(4) Oostergetel, G.; Amerongen, H.; Boekema, E. The Chlorosome: A Prototype for Efficient Light Harvesting in Photosynthesis. *Photosynth. Res.* **2010,** *104*, 245-255.

(5) Oostergetel, G. T.; Reus, M.; Gomez Maqueo Chew, A.; Bryant, D. A.; Boekema, E. J.; Holzwarth, A. R. Long-Range Organization of Bacteriochlorophyll in Chlorosomes of Chlorobium Tepidum Investigated by Cryo-Electron Microscopy. *FEBS Lett.* **2007,** *581*, 5435-9.

(6) Saga, Y.; Shibata, Y.; Itoh, S.; Tamiaki, H. Direct Counting of Submicrometer-Sized Photosynthetic Apparatus Dispersed in Medium at Cryogenic Temperature by Confocal Laser Fluorescence Microscopy: Estimation of the Number of Bacteriochlorophyll c in Single Light-Harvesting Antenna Complexes Chlorosomes of Green Photosynthetic Bacteria. *J. Phys. Chem. B* **2007,** *111*, 12605-12609.

(7) Jonas, D. M. Two-Dimensional Femtosecond Spectroscopy. *Annu. Rev. Phys. Chem.* **2003,** *54*, 425-463.

(8) Brixner, T.; Mancal, T.; Stiopkin, I. V.; Fleming, G. R. Phase-Stabilized Two-Dimensional Electronic Spectroscopy. *J. Chem. Phys.* **2004,** *121*, 4221-4236.

(9) Turner, D. B.; Dinshaw, R.; Lee, K.-K.; Belsley, M. S.; Wilk, K. E.; Curmi, P. M. G.; Scholes, G. D. Quantitative Investigations of Quantum Coherence for a Light-Harvesting Protein at Conditions Simulating Photosynthesis. *Phys. Chem. Chem. Phys.* **2012,** *14*, 4857-4874.

(10) Cheng, Y.-C.; Fleming, G. R. Coherence Quantum Beats in Two-Dimensional Electronic Spectroscopy. *J. Phys. Chem. A* **2008,** *112*, 4254-4260.

(11) Turner, D. B.; Wilk, K. E.; Curmi, P. M. G.; Scholes, G. D. Comparison of Electronic and Vibrational Coherence Measured by Two-Dimensional Electronic Spectroscopy. *J. Phys. Chem. Lett.* **2011,** *2*, 1904-1911.

(12) Kim, J.; Huxter, V. M.; Curutchet, C.; Scholes, G. D. Measurement of Electron−Electron Interactions and Correlations Using Two-Dimensional Electronic Double-Quantum Coherence Spectroscopy. *J. Phys. Chem. A* **2009,** *113*, 12122-12133.

(13) Nemeth, A.; Sperling, J.; Hauer, J.; Kauffmann, H. F.; Milota, F. Compact Phase-Stable Design for Single- and Double-Quantum Two-Dimensional Electronic Spectroscopy. *Opt. Lett.* **2009,** *34*, 3301-3303.

(14) Savikhin, S.; Zhu, Y.; Lin, S.; Blankenship, R. E.; Struve, W. S. Femtosecond

Spectroscopy of Chlorosome Antennas from the Green Photosynthetic Bacterium Chloroflexus Aurantiacus. *J. Phys. Chem.* **1994,** *98*, 10322-10334.
(15) Savikhin, S.; van Noort, P. I.; Zhu, Y.; Lin, S.; Blankenship, R. E.; Struve, W. S. Ultrafast Energy Transfer in Light-Harvesting Chlorosomes from the Green Sulfur Bacterium Chlorobium Tepidum. *Chem. Phys.* **1995,** *194*, 245-258.
(16) Savikhin, S.; van Noort, P. I.; Blankenship, R. E.; Struve, W. S. Femtosecond Probe of Structural Analogies between Chlorosomes and Bacteriochlorophyll c Aggregates. *Biophys. J.* **1995,** *69*, 1100-1104.
(17) Cherepy, N. J.; Du, M.; Holzwarth, A. R.; Mathies, R. A. Near-Infrared Resonance Raman Spectra of Chlorosomes: Probing Nuclear Coupling in Electronic Energy Transfer. *J. Phys. Chem.* **1996,** *100*, 4662-4671.
(18) Ma, Y. Z.; Aschenbrucker, J.; Miller, M.; Gillbro, T. Ground-State Vibrational Coherence in Chlorosomes of the Green Sulfur Photosynthetic Bacterium Chlorobium Phaeobacteroides. *Chem. Phys. Lett.* **1999,** *300*, 465-472.
(19) Prokhorenko, V. I.; Steensgaard, D. B.; Holzwarth, A. R. Exciton Dynamics in the Chlorosomal Antennae of the Green Bacteria Chloroflexus Aurantiacus and Chlorobium Tepidum. *Biophys. J.* **2000,** *79*, 2105-2120.
(20) Brixner, T.; Stenger, J.; Vaswani, H. M.; Cho, M.; Blankenship, R. E.; Fleming, G. R. Two-Dimensional Spectroscopy of Electronic Couplings in Photosynthesis. *Nature* **2005,** *434*, 625-628.
(21) Womick, J. M.; Moran, A. M. Exciton Coherence and Energy Transport in the Light-Harvesting Dimers of Allophycocyanin. *J. Phys. Chem. B* **2009,** *113*, 15747-15759.
(22) Myers, J. A.; Lewis, K. L. M.; Fuller, F. D.; Tekavec, P. F.; Yocum, C. F.; Ogilvie, J. P. Two-Dimensional Electronic Spectroscopy of the D1-D2-Cyt B559 Photosystem II Reaction Center Complex. *J. Phys. Chem. Lett.* **2010,** *1*, 2774-2780.
(23) Harel, E.; Engel, G. S. Quantum Coherence Spectroscopy Reveals Complex Dynamics in Bacterial Light-Harvesting Complex 2 (LH2). *Proc. Natl. Acad. Sci. U.S.A.* **2012,** *109*, 706-711.
(24) Milota, F.; Sperling, J.; Nemeth, A.; Abramavicius, D.; Mukamel, S.; Kauffmann, H. F. Excitonic Couplings and Interband Energy Transfer in a Double-Wall Molecular Aggregate Imaged by Coherent Two-Dimensional Electronic Spectroscopy. *J. Chem. Phys.* **2009,** *131*, 054510.
(25) Milota, F.; Sperling, J.; Nemeth, A.; Mančal, T.; Kauffmann, H. F. Two-Dimensional Electronic Spectroscopy of Molecular Excitons. *Acc. Chem. Res.* **2009,** *42*, 1364-1374.
(26) Barkhuijsen, H.; de Beer, R.; van Ormondt, D. Improved Algorithm for Noniterative Time-Domain Model Fitting to Exponentially Damped Magnetic Resonance Signals. *J. Magn. Reson.* **1987,** *73*, 553-557.
(27) Fujita, T.; Brookes, J. C.; Saikin, S. K.; Aspuru-Guzik, A. Memory-Assisted Exciton Diffusion in the Chlorosome Light-Harvesting Antenna of Green Sulfur Bacteria. *J. Phys. Chem. Lett.* **2012,** *3*, 2357-2361.